Multifunctional and superhydrophobic cellulose composite paper for electromagnetic shielding, hydraulic triboelectric nanogenerator and Joule heating applications

En Li [a,1], Yamin Pan [a,1], Chunfeng Wang [b], Chuntai Liu [a], Changyu Shen [a], Caofeng Pan [b], Xianhu Liu [a,*]

[a] College of Materials Science and Engineering, National Engineering Research Center for Advanced Polymer Processing Technology, Henan Province Industrial Technology Research Institute of Resources and Materials, Key Laboratory of Advanced Material Processing & Mold (Ministry of Education), Zhengzhou University, Zhengzhou 450002, China
[b] Beijing Institute of Nanoenergy and Nanosystems, Chinese Academy of Sciences, National Center for Nanoscience and Technology (NCNST), Beijing 100083, China

ARTICLE INFO

ABSTRACT

Cellulose-based materials have attracted tremendous interest recently due to their fascinating merits of renewability, biodegradability, and low cost, holding great promise in electromagnetic protection, clean energy harvesting, and thermal management. However, the simple and effective integration of multiple functions into single cellulose material remains a challenge. Herein, we report the fabrication of a multifunctional and superhydrophobic cellulose composite paper (CCP) via coated MXene modified by in-situ polymerized polypyrrole and PDMS/candle soot on the opposite surface of the paper. CCP exhibits high-performance electromagnetic interference shielding effectiveness (~40 dB) while maintaining high electrical conductivity (1467 S/m). Moreover, the superhydrophobic surface of CCP can be used as the hydraulic triboelectric nanogenerator (H-TENG) to harvest water energy due to the liquid–solid contact triboelectrification and electrostatic induction. The hydraulic triboelectric energy can be captured and released when water droplets drop from a height of 2 cm and roll at a tilt angle of 20°, the output current can reach a peak of 0.8 nA. Furthermore, the surface saturation temperature of CCP can reach 140 °C with a low applied voltage of 6 V enabled by the Joule effect. Thus, CCP holds great potentials in applications of integrated smart electronics, clean energy harvesting, and thermal management.

1. Introduction

With the development of miniaturized and highly integrated electronics, the additional requirements of shielding electromagnetic radiation, reserving clean energy, and seeking renewable electrothermal materials have been emerging for the life and health of human beings [1–7]. Thus, the multifunctional cellulose electromagnetic interference (EMI) shielding materials that can realize energy conversion and simultaneously surmount the aforementioned problems are highly desired [8,9]. In addition, triboelectric nanogenerator (TENG) was first invented by Wang in 2012 [10], based on the coupling effect of triboelectrification and electrostatic induction. Based on this, a recently emerging technology, hydraulic triboelectric nanogenerator (H-TENG)

appeared, which is a low cost, high efficiency, lightweight, and clean energy technology, has been developed as a hydro-energy harvester [11]. So far, the emergence of corrosion resistance, lightweight, easy processing, and low-cost polymer nanocomposite is a clear trend to supersede alternative metal-based EMI shielding materials [12–16]. Plentiful pioneering works have been dedicated to the fabrication of different types of active materials on cellulose bases through solution techniques, such as dip-coating [17], spraying [18], and vacuum filtration [19]. Currently, metal nanoparticles/nanowires [20,21], polypyrrole [22], polyaniline [23], carbon nanotubes [24,25], and graphene nanomaterials have been widely used in EMI shielding [26,27].

Recently, due to the excellent conductivity, hydrophilic, and outstanding mechanical properties, MXenes have attracted widespread

---

attention in energy storage [28], supercapacitor [29], strain sensing [30], thermal management [31,32], EMI shielding [33,34], and other fields [35–37]. During the etching and delamination process, abundant surface terminal groups had been introduced on the surface of the MXene sheets. This makes the surface inertness of MXene different from graphene. Accordingly, the thin MXene sheets interact with the cellulose-based network structure do not sacrifice the conductivity of the crystal, and this is a benefit to prepare the multifunctional polymer nanocomposites [38]. Huang et al. [17] demonstrated a MXene/cellulose nanocomposite paper with an EMI SE of 43 dB by dip-coating method. Ma et al. [8] prepared the ANF-MXene/AgNW nanocomposite paper by combining vacuum-assisted filtration and hot-pressing. The nanocomposite paper exhibited the EMI SE of 48.1 dB and the electrical conductivity of 922.0 S/cm. However, the functions of these papers are relatively single, not-addressed regarding the integration of various functions, and are weak in large-scale simple preparation. Wang and co-workers [11] developed a new type of drum-shaped triboelectric nanogenerator (D-TENG) with great superhydrophobic properties by coated SiO_2 on cellulose filter paper with the treatment of triethoxy-1H,1H,2H,2H-tridecafluoro-n-octylsilane ($C_{14}H_{19}F_{13}O_3Si$). The D-TENG generated the voltage output of 21.6 V and the charge transfer of 10 nC. This proves the application potential of cellulose filter paper in the field of harvesting water energy. However, the high content of fillers, the complex preparation process, and the high cost of the above composite paper materials have limited their wide application. Moreover, most existing water-based TENGs harvest devices are limited by low energy density. This is because the generation and transfer of interface charges mainly occur at the interface, but the contact area between water droplets and the interface is relatively small. The nucleation of nanometer water droplets or ice/frost during the operation of the device can cause unnecessary wetting transitions, shield effective charge generation and transmission, and significantly reduce energy collection efficiency [39].

The current issue faced by cellulose materials is how to expand new functionalities while enhancing its inherent performances. Herein, we demonstrate the CCP with high-performance EMI shielding, H-TENG, and Joule heating performances by coated with MXene/PPy ink and PDMS/candle soot on different surfaces. PPy on the surface and edges facilitate the MXene sheets form stable conductive ink for the strong protective coating on cellulose filter paper and further improve the EMI SE. PDMS has good corrosion resistance and hydrophobicity, and is often used as a surface protective coating [40]. After being combined with candle soot, it will have excellent superhydrophobicity [41]. Furthermore, by simply assembling the composite paper into a H-TENG, the energy of the water droplet rolling is harvested and output as an electrical signal. In addition, the MXene/PPy greatly improves the conductivity of the CCP, providing excellent Joule heating performance. Based on current practical applications, the deposition of ice can do harm to the mechanical properties and EMI performance of materials. Accordingly, excellent Joul heating performance and super-hydrophobicity of the CCP is endowed with high-speed deicing capability can provide potential for solving this problem.

2. Results and discussion

2.1. Fabrication of the highly conductive and stable MXene/PPy ink

Primarily, the delaminated MXene sheets were prepared by the minimally intensive layer delamination method with selective etching MAX (Ti_3AlC_2) in LiF/HCl mixture. MXene/PPy ink was fabricated via in-situ polymerization of pyrrole with no initiator in the suspension of MXene [30]. The Al layer in Ti_3AlC_2 was successfully etched away, as confirmed by XRD patterns of Fig. 1a. The diffraction peak of (002) shifts from 5.88° to 5.68° and a large decline confirmed the expansion of the spacing of the sheets. According to the formula: $2d\sin\theta = n\lambda$ (where d is the interplanar spacing, θ is the Bragg angle, n is the diffraction order, and λ is the wavelength of the X-ray (0.15 406 nm)), the interplanar spacing of delaminated $Ti_3C_2T_x$ MXene and MXene/PPy are about 15.01 Å and 15.55 Å, respectively. In addition, the peak of PPy appears to be relatively broad and weak, reflecting the amorphous
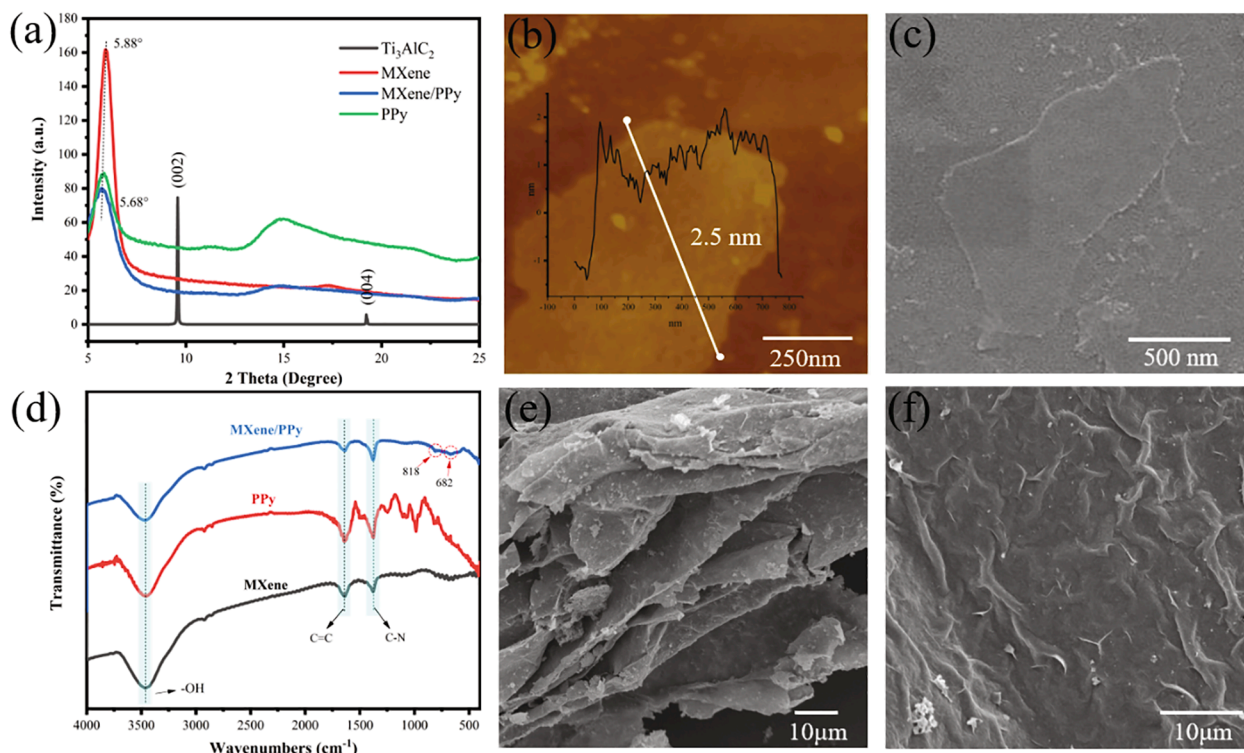
Fig. 1. (a) XRD patterns of Ti_3AlC_2, delaminated $Ti_3C_2T_x$ MXene, PPy, and MXene/PPy. (b, c) AFM and SEM images of the MXene sheet. (d) FTIR spectra of MXene, PPy, and MXene/PPy. (e) SEM image of delaminated MXene sheets, and (f) MXene/PPy composite.

structure of PPy. However, MXene/PPy has the characteristic diffraction pattern of $Ti_3C_2T_x$, and a weak and broad peak appears on the scale of 10–20°, which corresponds to the characteristic diffraction pattern of PPy [42]. AFM and SEM images exhibit the average thickness of about 2.5 nm and the morphology of the thin MXene sheets, respectively, as shown in Fig. 1b and c. The morphology of MXene sheets with a layer-by-layer configuration also demonstrates the expansion of the spacing of the sheets (Fig. 1e). From the SEM image of the MXene/PPy composite (Fig. 1f), the surface exhibits many bright white wavy shapes at the edge defects of the MXene sheets, which is the result of the modification of PPy.

The result of FTIR (Fig. 1d) also confirms the successful modification of PPy on the MXene surface and the formation of hydrogen bonds between them. The hydrogen bond (O—H) existing on the surface of MXene corresponds to 3436 cm^{-1}, which can be provided by the strong hydrogen-bonded O—H or extremely strong coordinated H_2O [43]. For PPy, the absorption peaks at 3436 cm^{-1} attributed to the presence of a large number of terminal hydroxyl groups on the N—H group on the pyrrole ring [44]. Due to C=C stretching vibrations, and the ring deformation of polaron (C—N), MXene/PPy has characteristic peaks of PPy at the same location which corresponds to 1641 and 1374 cm^{-1} [45]. In addition, the new marked peaks of MXene/PPy at 818 and 632 cm^{-1} correspond to the out-of-plane vibration of C—H. The above FTIR results show that the pyrrole was successfully polymerized on MXene,
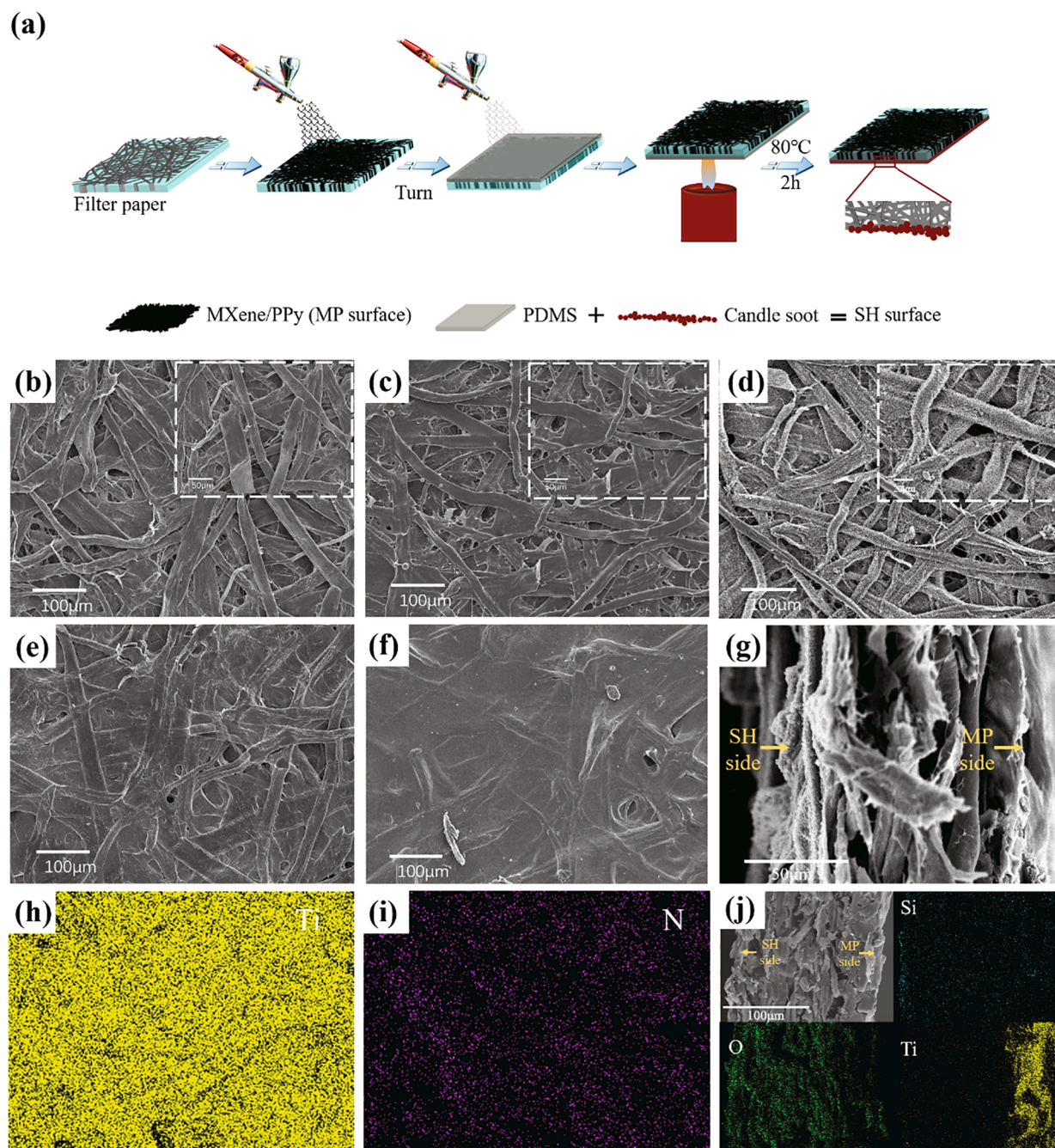
Fig. 2. (a) Schematic illustration of the fabrication of CCP. SEM images of the surface of (b) filter paper, (c) MP@P-P, (d) MP@SH-SH, (e) M−0.73, (f) MP@SH-MP, and (g) the cross-section of MP@SH (MP—MXene/PPy; SH—PDMS/candle soot; M—MXene; P—PDMS surface; MP@P-P represents the P side of MP@P, others are similar). (h, i) EDS elemental mapping images of (f). (j) SEM image and EDS elemental mapping images of the cross-section of MP@SH.

which is consistent with XRD results. Reportedly, MXene is easy to disperse in an aqueous solution because it is a hydrophilic substance with a negative surface charge [38]. The close contact between MXene and PPy is due to the opposite potential between them, which can provide a strong driving force to drive them to combine. Eventually, the excellent conductive and stable MXene/PPy ink can be formed, as demonstrated by the Tyndall effect (Fig. S1). The MXene/PPy also presents negative potential, which provides a possibility for the solid–liquid contact H-TENG [30]. MXene is prone to oxidation and degradation due to prolonged exposure to oxygenated environments, the modification of PPy on the surface can play a passivation role to ensure the stability and functionality of MXene for a long time [22,46]. Under the synergistic effect, MXene also can restrain the performance reduction for classical small anion doped (PPy) in air [47].

2.2. Morphologies of CCP

The fabrication process of CCP is schematically presented in Fig. 2a. Firstly, the MXene/PPy ink was sprayed on one side of the cellulose filter paper to form the MP side (1.46 mg/cm^2). Afterwards, the PDMS mixture solution was sprayed on the opposite side of the filter paper, and then candle soot was collected on the PDMS to form SH side. The resultant sample was named MP@SH, and MP@P represents the next

step of collecting candle soot was not carried out. The MXene ink was also sprayed according to the above method, and the sample was named M−x with x representing the surface density of MXene.

For filter paper as shown in Fig. 2b, the cellulose fibers with a width of 15–40 μm are randomly interlaced, and the surface is flat, while the surface coated with PDMS became smooth (Fig. 2c). However, the surface morphology of MP@SH-SH (Fig. 2d) is no different from that of a single SH sample (Fig. S2a). The candle soot particles are uniformly distributed on the surface of them. In Fig. 2e, the surface of M−0.73 is rough and dull, and there are many voids, which similar to the surface of M−1.46 (Fig. S2b). The void on the surface of M−0.73 is greatly reduced compared to the filter paper. In contrast to the surface of M−0.73 and M−1.46, MP@SH-MP exhibits slightly smoother fiber surfaces (Fig. 2f). The surface displays the spindle-shaped polypyrrole morphologies, which also demonstrated the successful polypyrrole recombination. Exactly, the narrow slits between the fibers are filled with MXene/PPy components, so those adjacent fibers are tightly connected to form a more perfect conductive network. The dense packaging structure attribute to the good combination between the MXene/PPy and fibers. As shown in Fig. 2g, the candle soot and MXene/PPy sheets are each coated on the two surfaces of the filter paper.

The distribution of MXene/PPy on the cellulose fiber surface can be observed by the EDS element mapping of MP@SH-MP (Fig. 2h, i). It
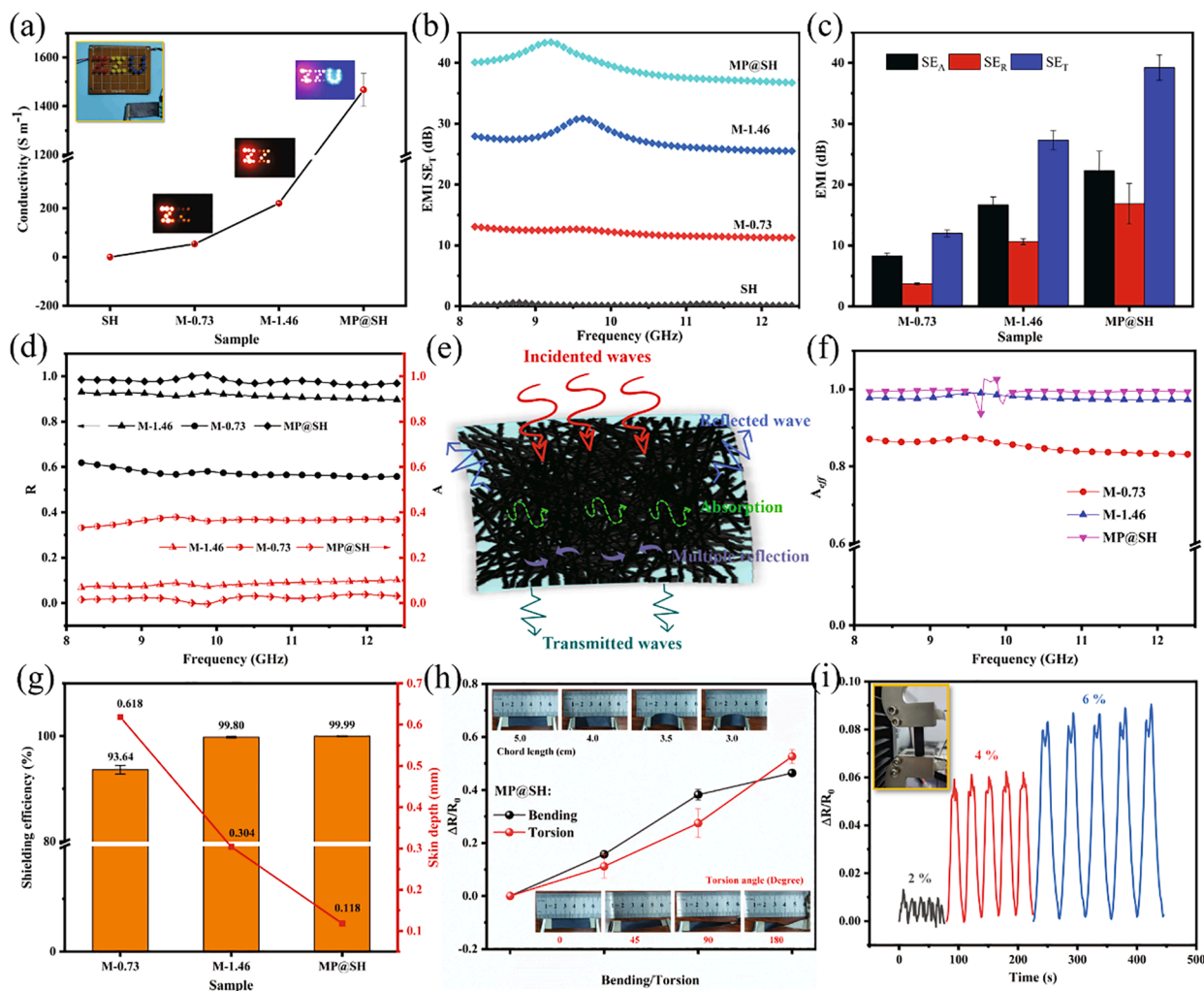
Fig. 3. (a) Electrical conductivity of CCP. (b) EMI SE$_T$ value of CCP in the X band. (c) Comparison of total EMI SE$_T$, SE$_A$, and SE$_R$ of CCP at the average frequency. (d) R and A of CCP in the X band. (e) Schematic of the EMI shielding mechanism of CCP. (f) A$_{eff}$ of CCP in the X band. (g) Change of EMI shielding efficiency and skin depth at 12.4 GHz of CCP. (h) Normalized relative resistance changes during bending and torsion tests, and (i) the resistance changes under various compression strains for MP@SH.

demonstrates that the titanium element (Ti) is distributed on the cellulose fiber surface uniformly. Meanwhile, nitrogen element (N) covers the whole cellulose fiber surface, proving that Py is well riveted on the fibers. EDS on the SH surface has been described in the previous report [41]. The SEM image of the cross-section of MP@SH and the corresponding EDS elemental mapping as shown in Fig. 2j. Obviously, the aggregation of Si and Ti elements can be seen on the SH and MP sides, respectively. Ti element had a permeation of ~ 40 μm inside the filter paper (Fig. S3), which is committed to the formation of the more complete conductive network in the cellulose filter paper.

2.3. Electrical and EMI shielding performances of CCP

The electrical conductivity of materials can be used as an important reference for predicting EMI shielding, in which conductivity is positively related to EMI SE [17,48,49]. Generally, highly conductive materials will produce larger induced currents under the action of electromagnetic waves (EMWs), these currents will weaken the penetration of EMWs according to Lenz's law [3]. As shown in Fig. 3a, SH is an insulator that coated PDMS/candle soot only. With the addition of PPy, the conductivity of MP@SH (1467 S/m) was much larger than that of M$-$1.46 (108 S/m) with the same surface density (1.46 mg/cm^2), due to formation of more conductive pathways [50,51]. Significantly, the multifunctional CCP reported in this study exhibits superior electrical conductivity and EMI SE to those cellulose fiber materials reported in the literature, as shown in Table S1. In the inset image of Fig. 3a, the circuit composed of MP@SH and LED bulb can be light up, which also demonstrates the high electrical conductivity of MP@SH. Fig. S4a shows the change in conductivity of the sample after being placed in the air for six months. The conductivity of MP@SH dropped to 885 S/m, while M$-$0.73 and M$-$1.46 dropped by more than half. This reflects the passivation effect of PPy on MXene in practical applications.

As shown in Fig. 3b, the EMI SE$_T$ of M$-$1.46 is about 27 dB in the whole X-band. Due to the outstanding electrical conductivity, MP@SH has an excellent EMI SE$_T$ of about 40 dB, which confirmed that PPy plays a pivotal role in electrical conductivity and EMI shielding performance. For M$-$0.73, the EMI SE$_T$ is significantly reduced to ~ 13 dB. The EMI SE$_T$ value of SH is no more than 0.5 dB, indicated that the SH hardly shields EMWs. Moreover, as shown in Fig. S4b, the EMI SE$_T$ of MP@SH changes ~ 5 dB after being placed in the air for six months. In order to explore the EMI shielding mechanism of the CCP in detail, the contributions of SE$_R$ and SE$_A$ to the SE$_T$ are analyzed (Fig. 3c). Meanwhile, Fig. 3d presents the values R and A of the obtained composite material. The value R increases with the increase of sample conductivity. The reason for the analysis is that impedance mismatch occurs as the conductivity increases [17]. When EMWs strike the surface of the composite material, a lot of reflections are immediately produced. In order to better understand the shielding mechanism of EMWs entering the interior of the composite material, their effective absorbance (A$_{eff}$) was calculated. As shown in Fig. 3f, more than 90% of the EMWs entered the composite material have been absorbed. Accordingly, absorption plays a leading role in the shielding mechanism of CCP. In addition, MP@SH possesses higher EMI shielding efficiencies of 99.98%, which can meet most application requirements (Fig. 3g). For the conductor, skin depth (δ) is a measure of depth at which the current density falls to 1/e, [17] which is expressed as:

$$\delta = \frac{1}{\sqrt{\pi f \mu \sigma}} \tag{1}$$

where f is the frequency, μ is the shield's magnetic permeability (μ = μ$_0$μ$_r$), μ$_0$ equals to $4\pi \times 10^{-7}$H/m, μ$_r$ is the shield's relative magnetic permeability and σ is the shield's electrical conductivity. Skin depth decreases with an increase in shield conductivity, according to previous literature [52]. The δ of MP@SH is 0.118 mm (δ ≤ d, d is the thickness of the sample), which also proves that the shielding mechanism is mainly

absorption [3].

In practical applications, the multifunctional CCP will inevitably have some deformations, such as folding, bending, and torsion, so satisfactory flexibility and structural stability are necessary. Fig. 3h displays the electrical resistance changes of MP@SH (10 × 50 mm^2) under bending and torsion. For MP@SH, the mutual stacking of MXene layers leads to more obvious resistance changes. When the torsion angle increased to 180°, ΔR/R$_0$ is about 50%. As the bending distance increased, the slope decreased and the final ΔR/R$_0$ was no more than 50%. The sensing performance of MP@SH (10 × 50 × 0.18 mm^3) was measured by a bending-strain test (inset image in Fig. 3i). The bending degree of the sensor can be calculated by ε = d/2R, R is the bending radius and ε is the bending strain [51,53,54]. Fig. 3i displays the sensor strain sensing behavior under cyclic load at different strain levels, and ΔR/R$_0$ value increased with the increase of strain. Each periodic peak of MP@SH is similar and seems to have potential applications in sensors. In addition, the long-term bending/release stability of MP@SH was evaluated at a 4% bending strain (Fig. S5). In the initial stage of the long-term stable cycle, the gradual increase in resistance may be due to the unrecoverable crack of the weakly brittle conductive path after bending and deformation.

2.4. Wettability and superhydrophobic hydraulic triboelectric nanogenerator

The excellent superhydrophobic property is the prerequisite for the use as a liquid–solid contact H-TENG [1]. Fig. 4a shows the water contact angles (WCAs) change between hydrophilic and hydrophobic surfaces. With the increase of MXene content, its hydrophilicity was also significantly improved. The WCA of MP@SH-MP is about 90°, which is larger than M$-$1.46. According to the results, the main reason is that the polymerization of PPy on MXene may make the MXene sheets denser and the MXene surface rougher. However, the opposite surface can be successfully converted to hydrophobic after being coated with PDMS/candle soot. Before the candle soot was collected, the surface of MP@P-P has a WCA of 142°. After that, the WCA of MP@SH-SH surface is 160°. The superhydrophobic behavior of the CCP with candle soot corresponds to the Cassie model [55,56]. Superhydrophobic surface of MP@SH-SH is also not contaminated by other liquids with color and viscosity, such as coffee, milk, black tea, and green tea (Fig. S6), and the CA were maintained at about 140° (Fig. 4b). Fig. S7 shows the robustness of the superhydrophobic surface of MP@SH-SH. The value of WCA after 20 repeated finger presses can be maintained at about 143°. The WCA of MP@SH-SH after rubbing a weight with a load of 50 g on sandpaper (1000 mesh) is about 138° (each movement distance is 5 cm). In addition, the MP@SH-SH has very low adhesion to water (Fig. 4c), and the water droplets can leave the sample surface (Fig. S8).

The internal structure and the operating principle of the superhydrophobic H-TENG are shown in Fig. 4d, e. The interdigital copper electrodes were adhered to between PTFE and glass to form an H-TENG substrate with a sandwich structure. MP@SH was attached to the surface of PTFE with double-sided adhesive, exposing the SH side to the air. In Fig. 4d, the process of harvesting energy was through releasing liquid droplets with different volumes rolling on the surface of MP@SH-SH at a tilt angle of 20°. The angle of 20° can make the water droplets come into contact with the superhydrophobic surface well during the rolling process and can avoid the water droplets bounce. The operating principles of H-TENG for harvesting water energy were demonstrated in Fig. 4e. Water droplets fall from the sky and generate a triboelectric charge, which is caused by being charged in contact with air or drifting particles [57]. When the positively charged water droplets reach the surface of the H-TENG, the positive charge shields the negative charge of the MP@SH-MP. Then, starting from the first electrode, charges of opposite polarity are induced on the adjacent interdigital electrodes [58–60]. Therefore, the unbalanced potential between the two electrodes drives the flow of free electrons from one electrode to the next until
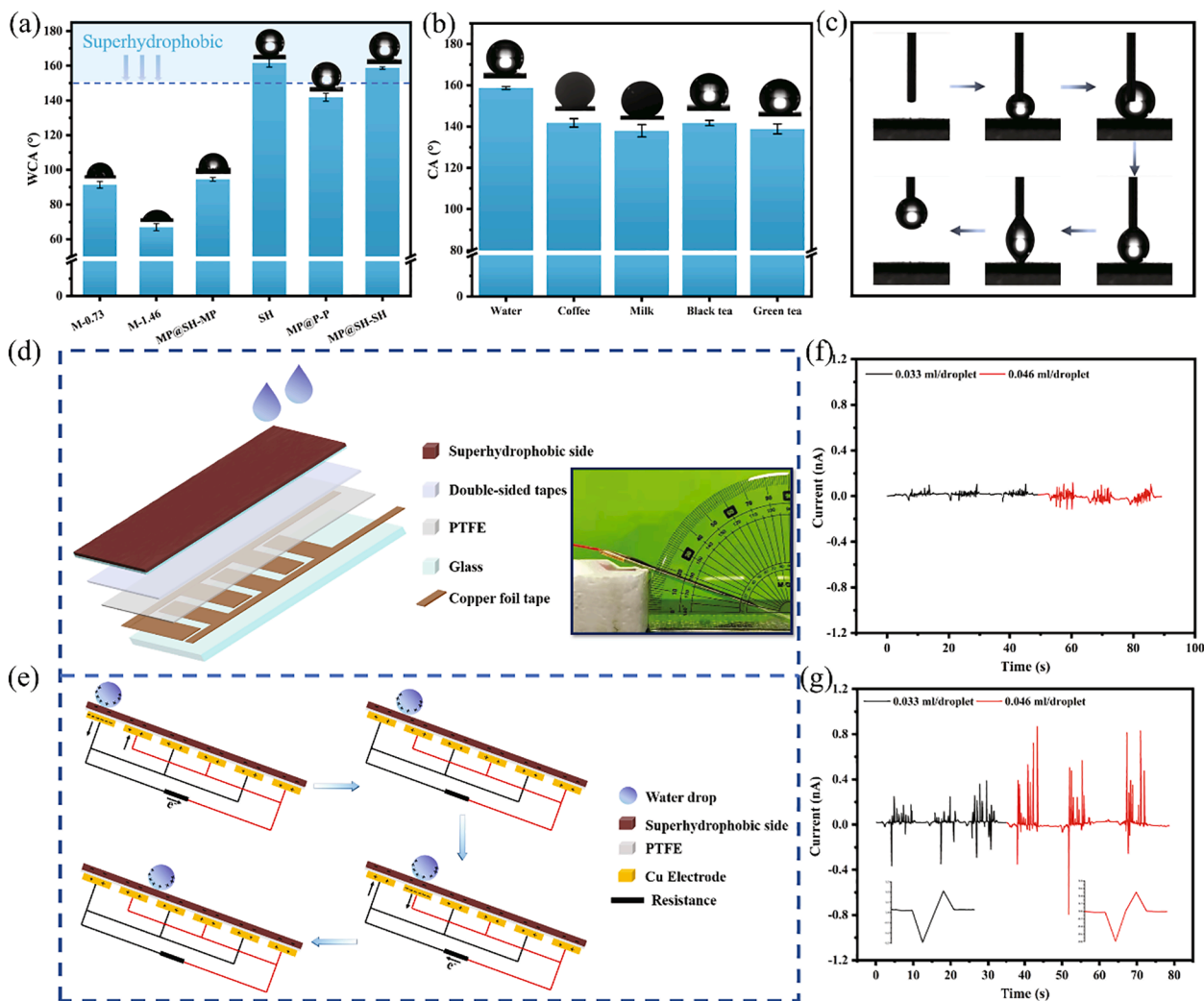
Fig. 4. (a) The measured WCA of the CCP on different surfaces. (b) CA of different droplets on the MP@SH-SH surface. (c) Picture of the MP@SH-SH surface with low water adhesion. (d) The structure of the H-TENG, and the physical picture of the tested sample. (e) Operating principle of the H-TENG. (f, g) The output current of the H-TENG generated by different volume water drops at the same dripping rates.

equilibrium is reached (Fig. 4e). As the water droplets continue to roll, free electrons continue to flow to the next electrode until the charge on the two electrodes reverses. If the water droplets keep touching and leaving H-TENG, it can provide continuous power output [1]. Accordingly, the cumulative charge generated by 10 droplets in each process was compared between two droplets of different volumes (0.033 mL/droplet and 0.046 mL/droplet) (Fig. 4g). Theoretically, the electrical output produced by these two solutions is not significant. As the volume of water droplets increased, the current response generated was more obvious. The corresponding single pulse current is shown in the inset of Fig. 4g. Interestingly, a single SH sample does not produce an obvious output current regardless of the volume of water droplets (Fig. 4f). This also explains well that the single SH sample cannot quickly transfer electrons. The low level of water energy produced by this H-TENG is owing to the design principle of the device and the limitation of the contact area of the liquid–solid interface and the low adhesion [39]. Such a design can be regarded as an open-circuit system, the charge generated by water contact was limited and separated from the output circuit, and the bottom electrode may impose unwanted screening effect [9]. However, the stability of TENG during use is a problem worthy of attention. The robustness of H-TENG is shown in Fig. S9. After pressing the surface of the MP@SH-SH with a finger with a force of 5 N for 20 times, the output current generated by the sliding of water droplets (0.046 mL/droplet) was not significantly reduced.

2.5. Joule heating performances of CCP

The attractive thermal management properties of the flexible and highly conductive CCP in electric heater applications can be exploited. Fig. 5 shows the electrothermal conversion performance of the MP@SH (20×50 mm^2) under different stable input voltages. As shown in Fig. 5a, the linear I-V curve of MP@SH paper shows the low resistance, assuring the cellulose-based electric heater is safe and reliable when operating on the human body. Fig. 5b shows the change of CCP surface temperature with time at the low employed voltages from 1 to 6 V. No obvious surface temperature changes are observed under a voltage of 1 V. Nevertheless, the high saturation temperature of about 40 °C is generated under 2 V, which is further raised to 79 and 140 °C at 4 and 6 V, respectively. The heat generated by Joule heating is in accordance with Joule's law ($Q = U^2/R \cdot t$), so electrical conductivity is an important factor that affects the Joule heating ability, and the temperature plateau is also affected by the voltage. As shown in Fig. S10, the platform temperature between the dashed lines has a linear relationship with U^2. At a constant voltage of 4 V, after the 1st, 5th, 10th, and 20th heating/cooling cycles, the temperature curves do not change dramatically (Fig. 5c), indicating that the MP@SH paper heater has certain stability in circulation. Fig. 5d shows that the surface temperatures of the composite paper can be switched by tailoring the driving voltage from 1 to 6 V or from 6 to 1 V on account of the highly responsive. The surface
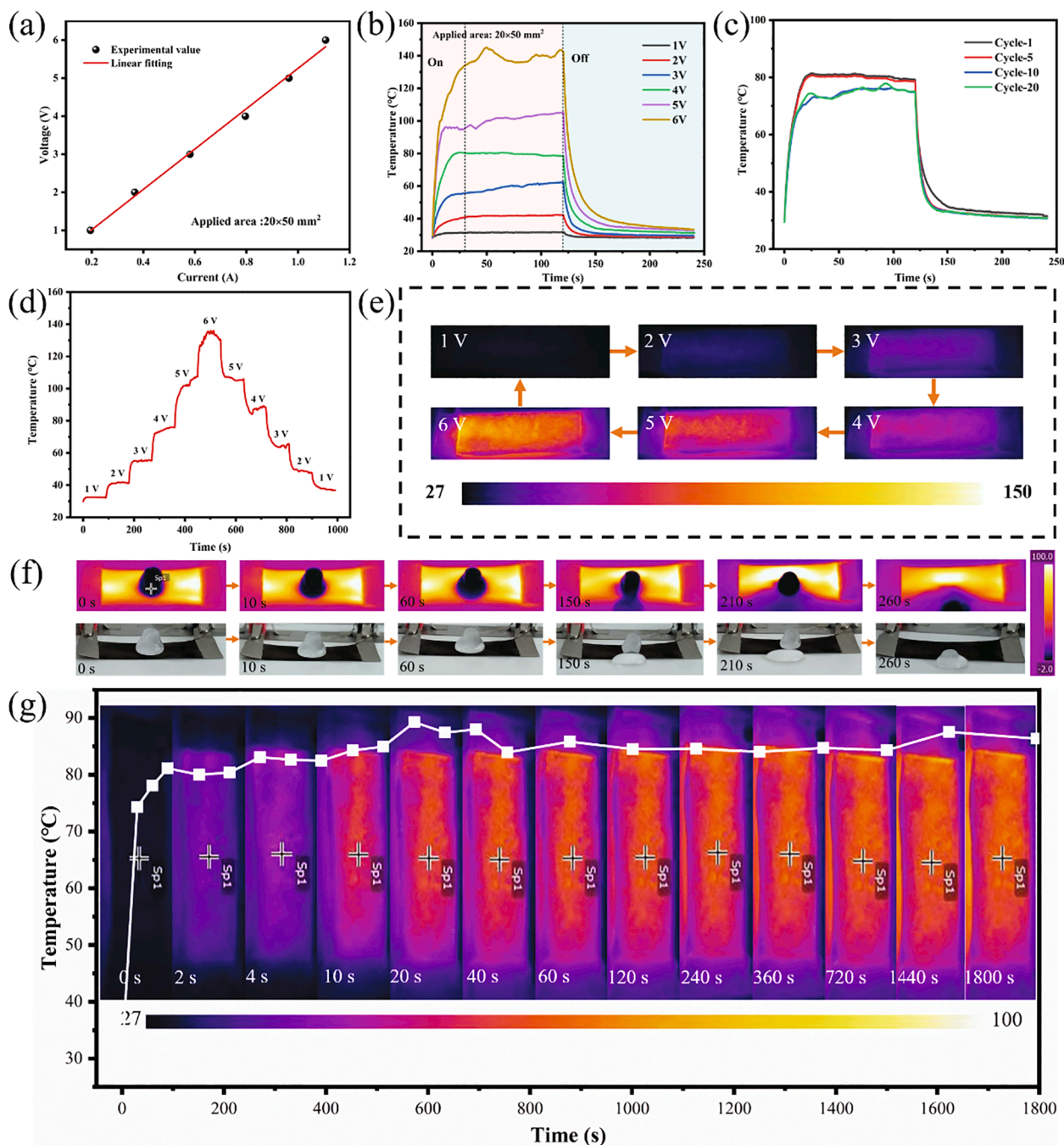
Fig. 5. Joule Heating Performances of MP@SH. (a) I-V curve and (b) Time–temperature curves from 1 to 6 V. (c) Temperature-stability during heating/cooling cycles. (d) Temperature evolution under stepwise increased/decreased power inputs. (e) IR images at the saturated temperature under different voltages. (f) IR and digital images of the ice/water at different times during the deicing process. (g) Temperature stability at a constant voltage of 4 V.

temperature of MP@SH increases rapidly with the increase of the driving voltage, and the controllability of the electric heating performance is thus demonstrated. Obviously, the temperature distribution on the sample surface may be related to the fiber structure and the distribution of conductive active materials (Fig. 5e).

The CCP electric heater can quickly reach the saturation temperature even under low voltage and short response time, thus ensuring the safety and normal application to the human body. The performance of the composite paper can not only be used to keep warm but also can be used for multiple purposes such as thermotherapy and deicing in icy and snowy weather. We placed a small ice cube (~1 cm^3) on the superhydrophobic side of the MP@SH, applied a constant voltage of 5 V to the sample by a DC power, and recorded the ice melting over different periods. As shown in Fig. 5f, the ice cubes slowly melted as the bottom temperature increased, completely melted within 260 s, and finally slipped off the surface of MP@SH-SH. Therefore, the CCP electric heater in this study retains heating property while also has excellent superhydrophobic, which can be used in many fields. Furthermore, after reaching the saturation temperature, the temperature of the heater was stable around 85 °C for a long time in 1800 s, which proves the electric heater can maintain satisfactory stability during the long-term healing process (Fig. 5g). Accordingly, the flexible multifunctional CCP has great potential in the application of thermal management devices, such as thermotherapy devices and heating deicing applications.

3. Conclusion

In conclusion, we demonstrated a flexible CCP with outstanding EMI SE, superhydrophobic liquid–solid H-TENG, and Joule heating performance through coating MXene/PPy and PDMS/candle soot on different surfaces of cellulose filter paper. In situ polymerized PPy is introduced on MXene surfaces to generate stable ink. The modification of PPy promotes the interface bondings between MXene and fibers, improves EMI SE and conductivity. The MP@SH exhibits a high electrical conductivity of 1467 S/m and an excellent EMI SE of 40 dB. In addition, based on superhydrophobic property, the CCP has the potential of a liquid–solid H-TENG, which can generate a stable current output. Finally, the CCP shows an outstanding Joule heating temperature of about 140 °C at 6 V, also presented good heating stability and reliability. We believe that this facile and efficient strategy can produce CCP with excellent EMI SE, water droplet energy storage, and thermal management performance for high-tech applications in intelligent electronics and clean energy resources.

4. Experiment section

4.1. Materials

Ti_3AlC_2 MAX (400 mesh, greater than98% purity) powder was obtained from Jilin 11 Technology Co., Ltd. Lithium fluoride (LiF, 99%) and pyrrole (Py, 99%) were provided by Shanghai Aladdin Biochemical Technology Co., Ltd. Hydrogen chloride (HCl, 37 wt%, AR) was gained from Sinopharm Chemical Reagent Co., Ltd. (China). Isopropanol and ethanol (C_2H_5OH) and xylene (purity 99%) were offered by Tianjin Damao Chemical Reagent Co., Ltd, respectively. Candles were purchased from the local shop. The filter paper was gained from the Liaoning Fushun Filter Paper factory. PDMS (Sylgard 184) and the curing agent were obtained from Dow Corning, U.S.A.

4.2. Preparation of $Ti_3C_2T_x$ MXene sheets

$Ti_3C_2T_x$ MXene sheets were prepared by the minimally intensive layer delamination (MILD) method through etching of MAX (Ti_3AlC_2) powders as reported [61]. Specifically, 2 g LiF and 40 mL HCl (9 M) were mixed by stirring at room temperature for 30 min. Then, 2 g Ti_3AlC_2 MAX was slowly added and stirred for 24 h (400 rpm) at the temperature of 35 °C. This process is the etching of the Al element to obtain multilayer $Ti_3C_2T_x$. The precipitation obtained needs to be washed with deionized water after centrifugation at 3500 rpm for 10 min until the PH of the supernate reaches about 6. After that, the obtained multilayer sediment was dispersed into 120 mL ethanol for delamination and sonicated for 1 h to get delaminated $Ti_3C_2T_x$. The resulting suspension was centrifuged at 3500 rpm for 3 min for collecting the homogeneous supernatant. Finally, delaminated $Ti_3C_2T_x$ MXene sheets were obtained after 72 h of freeze-drying.

4.3. Preparation of MXene/PPy ink

MXene/PPy ink was fabricated via in-situ polymerization of pyrrole with no initiator in the suspension of MXene. Typically, to obtain a homogeneous MXene dispersion solution (6 mg/mL), 0.15 g MXene sheets were dissolved in 25 mL deionized water and sonicated for 30 min. 0.1515 g Pyrrole was added in 5 mL isopropyl alcohol form a light-yellow transparent solution. Then, the resultant solution was dropped into the MXene dispersion solution and stirred at room temperature for 12 h. Finally, the homogeneous MXene/PPy ink (5 mg/mL) was obtained. The concentration of the ink was confirmed by weighing the remaining solid weight after drying a known volume of suspension filtered through a polypropylene membrane with a pore size of 0.45 μm. For comparison, the MXene ink (5 mg/mL) of the same concentration was also configured according to the above method.

4.4. Preparation of CCP

The filter paper was coated with MXene/PPy ink (5 mg/mL) by the spray-coating method through a commercial spray (Airbrush WeiYi HD180). Firstly, 2.92 mL MXene/PPy ink was uniformly spray-coated onto one side of filter paper, then dry in a vacuum oven at 50 °C for 10 min (Surface density: 1.46 mg/cm²). PDMS, Xylene, and curing agent with a volume rate of 10:50:1 were mixed by stirring for 40 min [35]. Afterward, the prepared PDMS mixture was spray-coated on the opposite side of the above paper for 5 s. After that, place the side sprayed with PDMS above the candle flame and move it quickly to collect the candle soot. This process lasts about 30 s and the distance from the center of the candle flame is about 10–15 mm. In the end, the prepared sample was placed in an oven at 80 °C for 2 h. For convenience, the sample was named MP@SH. MP@P means that no candle soot was collected. The MXene ink was also sprayed according to the above method, and the sample was named M−x with x representing the surface density of MXene is 0.73 mg/cm² or 1.46 mg/cm².

4.5. Characterization

The morphology and thickness of the MXene sheet were characterized by scanning probe atomic force microscope (AFM, Bruker Multi-Mode 8). Morphologies and microstructures of $Ti_3C_2T_x$ MXene, as well as the composite papers, were observed with field emission scanning electron microscope (FE-SEM, JSM-7001F). The chemical elements of the samples were characterized by EDS (Energy Dispersive Spectrometer). X-Ray Diffraction (XRD) patterns were obtained using D8 Wide-Angle X-Ray Diffractometer (Bruker, Germany) at a scanning rate of 4°/min. The FTIR spectrum was obtained using an FTIR spectrometer (Thermo Fisher Nicolet 6700, USA) in the range of 4000–400 cm^{-1}. The conductivity of multifunctional CCP was calculated by this formula: $\sigma = \frac{L}{SR}$ (where L is the length, S is the area of cross-sectional, and R is the resistance). A Digital multimeter (Tektronix DMM4050) was used to measure the resistance of CCP. RST 5000 electrochemical workstation was used as the main instrument for current–time (I-t) measurement when water droplets roll on the surface of MP@SH. Stable input voltages were supplied by a DC power (UTP 1306S, UNI-T), and the temperature on the sample surface was recorded via a thermal imaging camera (E60, FLIR).

The EMI SE was measured via a vector network analyzer (Agilent N5244A) within 8.2–12.4 GHz (X-Band) based on the waveguide method. S_{11} and S_{21} are scattering parameters for calculating the power coefficients of reflection (R), transmission (T), and absorption (A). The total electromagnetic shielding (SE_T) is calculated using the following equation:

$$R = |S_{11}|^2 \tag{2}$$

$$T = |S_{21}|^2 \tag{3}$$

$$SE_R = -10\log(1-R) \tag{4}$$

$$SE_A = -10\log(T/1-R) \tag{5}$$

$$SE_T = SE_R + SE_A \tag{6}$$

where SE_R is the microwave reflection, SE_A is the microwave absorption, and SE_T is the total EMI SE. When $SE_T > 15$ dB, SE_M (The multilayer reflection) can be negligible [62]. The EMI shielding efficiency (%) under 12.4 GHz is obtained by the following equation:

$$\text{shielding efficiency}(\%) = 100 - \left(\frac{1}{10^{\frac{SE_T}{10}}}\right) \times 100 \tag{7}$$

Declaration of Competing Interest

The authors declare that they have no known competing financial interests or personal relationships that could have appeared to influence the work reported in this paper.

Acknowledgments

Appendix A. Supplementary data

Supplementary data to this article can be found online at https://doi.org/10.1016/j.cej.2021.129864.

References

[1] Q. Zhang, Q. Liang, Q. Liao, M. Ma, F. Gao, X. Zhao, Y. Song, L. Song, X. Xun, Y. Zhang, Adv. Funct. Mater. 28 (2018) 1803117.
[2] G.M. Weng, J. Li, M. Alhabeb, C. Karpovich, H. Wang, J. Lipton, K. Maleski, J. Kong, E. Shaulsky, M. Elimelech, Y. Gogotsi, A.D. Taylor, Adv. Funct. Mater. 28 (2018) 1803360.
[3] C. Wang, V. Murugadoss, J. Kong, Z. He, X. Mai, Q. Shao, Y. Chen, L. Guo, C. Liu, S. Angaiah, Z. Guo, Carbon 140 (2018) 696–733.
[4] Q. Li, Z. Zhang, L. Qi, Q. Liao, Z. Kang, Y. Zhang, Adv. Sci. 6 (2019) 1801057.
[5] T. Yun, H. Kim, A. Iqbal, Y.S. Cho, G.S. Lee, M.K. Kim, S.J. Kim, D. Kim, Y. Gogotsi, S.O. Kim, C.M. Koo, Adv. Mater. 32 (2020), e1906769.
[6] Q. Wei, S. Pei, X. Qian, H. Liu, Z. Liu, W. Zhang, T. Zhou, Z. Zhang, X. Zhang, H. M. Cheng, W. Ren, Adv. Mater. 32 (2020), e1907411.
[7] X.J. Zha, X. Zhao, J.H. Pu, L.S. Tang, K. Ke, R.Y. Bao, L. Bai, Z.Y. Liu, M.B. Yang, W. Yang, ACS Appl. Mater. Interfaces 11 (2019) 36589–36597.
[8] Z. Ma, S. Kang, J. Ma, L. Shao, Y. Zhang, C. Liu, A. Wei, X. Xiang, L. Wei, J. Gu, ACS Nano 14 (2020) 8368–8382.
[9] W. Xu, H. Zheng, Y. Liu, X. Zhou, C. Zhang, Y. Song, X. Deng, M. Leung, Z. Yang, R. X. Xu, Z.L. Wang, X.C. Zeng, Z. Wang, Nature 578 (2020) 392–396.
[10] F.R. Fan, Z.Q. Tian, Z. Lin Wang, Nano Energy 1 (2012) 328–334.
[11] S. Nie, H. Guo, Y. Lu, J. Zhuo, J. Mo, Z.L. Wang, Adv. Mater. Technol. 5 (4) (2020) 2000454.
[12] H. Abbasi, M. Antunes, J.I. Velasco, Prog. Mater. Sci. 103 (2019) 319–373.
[13] Z. Zeng, H. Jin, M. Chen, W. Li, L. Zhou, Z. Zhang, Adv. Funct. Mater. 26 (2016) 303–310.
[14] C. Liang, P. Song, H. Qiu, Y. Huangfu, Y. Lu, L. Wang, J. Kong, J. Gu, Compos. Pt. A-Appl. Sci. Manuf. 124 (2019), 105512.
[15] N. Yousefi, X. Sun, X. Lin, X. Shen, J. Jia, B. Zhang, B. Tang, M. Chan, J.K. Kim, Adv. Mater. 26 (2014) 5480–5487.
[16] W.L. Song, X.T. Guan, L.Z. Fan, W.Q. Cao, C.Y. Wang, Q.L. Zhao, M.S. Cao, J. Mater. Chem. A 3 (2015) 2097–2107.
[17] D. Hu, X. Huang, S. Li, P. Jiang, Compos. Sci. Technol. 188 (2020), 107995.
[18] X. Zhang, X. Wang, Z. Lei, L. Wang, M. Tian, S. Zhu, H. Xiao, X. Tang, L. Qu, ACS Appl. Mater. Interfaces 12 (2020) 14459–14467.
[19] F. Xie, F. Jia, L. Zhuo, Z. Lu, L. Si, J. Huang, M. Zhang, Q. Ma, Nanoscale 11 (2019) 23382–23391.
[20] L.X. Liu, W. Chen, H.B. Zhang, Q.W. Wang, F. Guan, Z.Z. Yu, Adv. Funct. Mater. 29 (2019) 1905197.
[21] B. Zhao, J.S. Deng, R. Zhang, L.Y. Liang, B.B. Fan, Z.Y. Bai, G. Shao, C.B. Park, Eng. Sci. 3 (2018) 5–40.
[22] P.P. Deshpande, N.G. Jadhav, V.J. Gelling, D. Sazou, J. Coat. Technol. Res. 11 (2014) 473–494.
[23] H. Sun, S. Xie, Y. Li, Y. Jiang, X. Sun, B. Wang, H. Peng, Adv. Mater. 28 (2016) 8431–8438.
[24] Y.J. Wan, X.Y. Wang, X.M. Li, S.Y. Liao, Z.Q. Lin, Y.G. Hu, T. Zhao, X.L. Zeng, C. H. Li, S.H. Yu, P.L. Zhu, R. Sun, C.P. Wong, ACS Nano 14 (2020) 14134–14145.
[25] M. Feng, Y. Pan, M. Zhang, Q. Gao, C. Liu, C. Shen, X. Liu, Compos. Sci. Technol. 206 (2021), 108666.
[26] L. Qiu, D. Li, H.M. Cheng, ACS Nano 12 (2018) 5085–5092.
[27] Z. Zeng, H. Jin, M. Chen, W. Li, L. Zhou, X. Xue, Z. Zhang, Small 13 (2017) 1701388.
[28] L. Shao, J. Xu, J. Ma, B. Zhai, Y. Li, R. Xu, Z. Ma, G. Zhang, C. Wang, J. Qiu, Compos. Commun. 19 (2020) 108–113.
[29] Y.Z. Wang, Y.X. Liu, C. Wang, H. Liu, J.X. Zhang, J. Lin, J.C. Fan, T. Ding, J.E. Ryu, Z.H. Guo, Eng. Sci. 9 (2020) 50–59.
[30] Q.W. Wang, H.B. Zhang, J. Liu, S. Zhao, X. Xie, L. Liu, R. Yang, N. Koratkar, Z. Z. Yu, Adv. Funct. Mater. 29 (2019) 1806819.
[31] W.T. Cao, C. Ma, D.S. Mao, J. Zhang, M.G. Ma, F. Chen, Adv. Funct. Mater. 29 (2019) 1905898.
[32] D.B. Zhang, S. Hu, Y.J. Sun, X. Liu, H.Y. Wang, H. Wang, Y.Z. Chen, Y.X. Ni, ES Energy Environ. 10 (2020) 59–65.
[33] Y. Zhang, L. Wang, J. Zhang, P. Song, Z. Xiao, C. Liang, H. Qiu, J. Kong, J. Gu, Compos. Sci. Technol. 183 (2019), 107833.
[34] H. Cheng, Y. Pan, Q. Chen, R. Che, G. Zheng, C. Liu, C. Shen, X. Liu, Adv. Compos. Hybrid Mater. 4 (2021), https://doi.org/10.1007/s42114-021-00224-1.
[35] L. Li, S. Zhao, X.J. Luo, H.B. Zhang, Z.Z. Yu, Carbon 10 (2020) 090.
[36] W. Chen, L.X. Liu, H.B. Zhang, Z.Z. Yu, ACS Nano 14 (2020) 16643–16653.
[37] P. Yang, H.X. Zhao, Y.N. Yang, P.X. Zhao, X.C. Zhao, L.J. Yang, E.S. Mater, Manuf. 7 (2020) 34–39.
[38] B. Akuzum, K. Maleski, B. Anasori, P. Lelyukh, N.J. Alvarez, E.C. Kumbur, Y. Gogotsi, ACS Nano 12 (2018) 2685–2694.
[39] W. Xu, Z. Wang, Joule 4 (2020) 2527–2531.
[40] J.P. Liu, J.X. Zhang, J.J. Tang, Y.L.X.L.Y. Pu, M.Q. Lu, L. Xu, Z.H. Guo, E.S. Mater, Manuf. 10 (2020) 29–38.
[41] X. Liu, X. Zhang, Q. Chen, Y. Pan, C. Liu, C. Shen, Chem. Eng. J. 406 (2021), 126532.
[42] K. Xie, J. Yin, H. Shi, Q. Zhu, P. Wu, Y. Tang, Y. Zhou, T. Lu, Ionics 21 (2014) 359–364.
[43] S. Xu, G. Wei, J. Li, Y. Ji, N. Klyui, V. Izotov, W. Han, Chem. Eng. J. 317 (2017) 1026–1036.
[44] M. Boota, B. Anasori, C. Voigt, M.Q. Zhao, M.W. Barsoum, Y. Gogotsi, Adv. Mater. 28 (2016) 1517–1522.
[45] Q. Liao, H. Hou, X. Liu, Y. Yao, Z. Dai, C. Yu, D. Li, J. Phys. Chem. Solids 115 (2018) 233–237.
[46] H. Ghassemi, W. Harlow, O. Mashtalir, M. Beidaghi, M.R. Lukatskaya, Y. Gogotsi, M.L. Taheri, J. Mater. Chem. A 2 (2014) 14339.
[47] K. Qi, Y. Qiu, Z. Chen, X. Guo, Corros. Sci. 60 (2012) 50–58.
[48] Y. Jia, R. Sun, Y. Pan, X. Wang, Z. Zhai, Z. Min, G. Zheng, C. Liu, C. Shen, X. Liu, Compos. Pt. B-Eng. 210 (2021), 108668.
[49] Q. Gao, Y. Pan, G. Zheng, C. Liu, C. Shen, X. Liu, Adv. Compos. Hybrid Mater. (2021) 4, https://doi.org/10.1007/s42114-021-00221-4.
[50] T.W. Lee, S.E. Lee, Y.G. Jeong, Compos. Sci. Technol. 131 (2016) 77–87.
[51] X. Wang, X. Liu, D.W. Schubert, Nano-Micro Lett. 13 (2021), 64.
[52] M.H. Al-Saleh, U. Sundararaj, Carbon 47 (2009) 1738–1746.
[53] S.J. Kim, W. Song, Y. Yi, B.K. Min, S. Mondal, K.S. An, C.G. Choi, ACS Appl. Mater. Interfaces 10 (2018) 3921–3928.
[54] H. Sun, Y. Zhao, C. Wang, K. Zhou, C. Yan, G. Zheng, J. Huang, K. Dai, C. Liu, C. Shen, Nano Energy 76 (2020), 105035.
[55] S.B.A.B.D. Cassle, Trans. Faraday Soc. 40 (1944) 546–551.
[56] L.M.X. Deng, H.J. Butt, D. Vollmer, Science 335 (2012) 67–70.
[57] Q. Liang, X. Yan, Y. Gu, K. Zhang, M. Liang, S. Lu, X. Zheng, Y. Zhang, Sci. Rep. 5 (2015) 9080.
[58] D. Choi, D.W. Kim, D. Yoo, K.J. Cha, M. La, D.S. Kim, Nano Energy 36 (2017) 250–259.
[59] S. Hu, Z. Shi, R. Zheng, W. Ye, X. Gao, W. Zhao, G. Yang, ACS Appl. Mater. Interfaces 12 (2020) 40021–40030.
[60] J. Xiong, M.F. Lin, J. Wang, S.L. Gaw, K. Parida, P.S. Lee, Adv. Energy Mater. 7 (2017) 1701243.
[61] Q. Gao, M. Feng, E. Li, C. Liu, C. Shen, X. Liu, Macromol. Mater. Eng. (2020) 2000343.
[62] Y. Liu, K. Zhang, Y. Mo, L. Zhu, B. Yu, F. Chen, Q. Fu, Compos. Sci. Technol. 168 (2018) 28–37.